Reciprocal-space approach to dipolarly coupled magnetic heterostructures

A. Del Giacco,[1,2,3,*,†] L. Menna,[4,5,*] M. J. Gross,[6] O. Wojewoda,[1,7] V. Levati,[2] M. Urbánek,[7] S. Kurdi,[5] E. Albisetti,[2] D. Petti,[2] and C. A. Ross[1]

[1]*Department of Materials Science and Engineering, Massachusetts Institute of Technology, Cambridge, Massachusetts 02139, USA*
[2]*Department of Physics, Politecnico di Milano, Piazza Leonardo da Vinci 32, Milan 20133, Italy*
[3]*Institute for NanoSystems Innovation (NanoSI), Northeastern University, Boston, Massachusetts 02115, USA*
[4]*Department of Physics, Politecnico di Milano, Piazza Leonardo da Vinci 32, Milan 20133, Italy*
[5]*Institute of Photonics and Quantum Sciences, SUPA, Heriot-Watt University, Edinburgh EH14 4AS, United Kingdom*
[6]*Department of Electrical Engineering and Computer Science, Massachusetts Institute of Technology, Cambridge, Massachusetts 02139, USA*
[7]*CEITEC BUT, Brno University of Technology, Brno, Czech Republic*

(Received 9 May 2026; revised 3 August 2026; accepted 28 September 2026; published 23 October 2026)

We present an analytical framework capable of describing spin-wave dynamics in magnetic heterostructures composed of a pair of exchange-decoupled magnetic layers separated by a nonmagnetic spacer, focusing in particular on garnet-based multilayers. The model captures the formation of collective spin-wave modes, namely symmetric and antisymmetric, arising from dipolar coupling and provides direct access to the dispersion relation of the system and consequent interference phenomena. This formalism establishes a versatile theoretical tool for the predictive design of dipolarly coupled magnonic devices, providing access to their eigenfrequencies and mode shapes.

DOI: 10.1103/9z24-jjx3

I. INTRODUCTION

The design of magnetic heterostructures lies at the core of spintronics and nanomagnetism. Central to this effort is the ability to engineer spin transport through careful control of interfacial properties, material selection, and layer composition [1–9]. Such heterostructures represent a versatile platform for engineering the magnonic dispersion relation and introduce tailored magnetic anisotropies capable of breaking spin-wave reciprocity, enabling compact and reconfigurable magnonic devices that offer directional control, signal routing, and interference-based functionalities [10–19]. Their theoretical description builds upon foundational studies of single-layer thin-film magnets [20,21] and it has been progressively extended to multilayered systems [14,22–26].

In this work, we focus on magnetic heterostructures composed of two exchange-decoupled magnetic layers separated by a nonmagnetic spacer, describing their collective behavior and its dependence on the dipolar coupling. The nontrivial form of the interaction leads to the formation of collective spin-wave modes. Higher and lower frequency branches naturally emerge in the dispersion modes, accompanied by range of effects including interference phenomena [27,28] and tunable energy transfer. Consistent with previous studies on lateral dipolarly coupled waveguides [28] and with vertical backward-volume configurations in permalloy heterostructures [29], vertically stacked magnetic systems support the simultaneous excitation of spin-wave eigenmodes characterized by different wave vectors k_s and k_{as}, at fixed frequency (ω^*), corresponding to collective symmetric and antisymmetric oscillations. Their resulting wave vector separation $\Delta k_x = k_s(\omega^*) - k_{as}(\omega^*)$ leads to interference and a transfer of energy between the two magnetic layers over a coupling length $L_{\text{coupling}}(\omega^*) \approx \pi/|\Delta k_x(\omega^*)|$. The resulting spatial modulation of the averaged spin-wave intensity arises from this coupled dynamics.

Stacking of magnetic layers along the out-of-plane direction introduces a nontrivial behavior of the global demagnetizing tensor of the system. This problem cannot be treated as a simple lifting of the degeneracy of the single-layer modes. Such an approach fails to capture the spatially coupled nature of the dipolar interaction and its

*These authors equally contribute to the study.
†Contact author: andreadg@mit.edu

Published by the American Physical Society under the terms of the Creative Commons Attribution 4.0 International license. Further distribution of this work must maintain attribution to the author(s) and the published article's title, journal citation, and DOI.

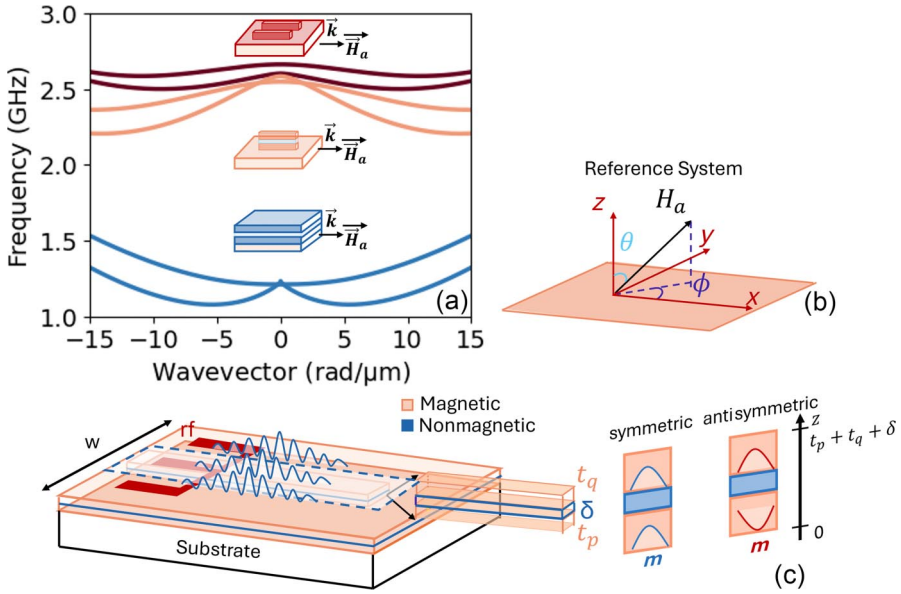


FIG. 1. (a) Comparison of the spin-wave dispersion relation between laterally coupled waveguides (red), vertically coupled heterostructure waveguides (orange), and an infinite film heterostructure (blue), in backward-volume configuration. The vertical heterostructure (blue and orange) is calculated for YIG(100 nm)/NM(50 nm)/YIG(100 nm) in which the vertical waveguides have a width $w = 100$ nm. The lateral waveguide configuration (red) has two waveguides of thickness $t = 50$ nm of YIG separated by 100 nm. The applied external field is $\mu_0 H_a = 10$ mT. (b) Schematic of the reference frames employed in the study: **x** is the longitudinal propagation direction, **y** is the transverse direction along the width (w) of the sample, **z** is the out-of-plane direction, θ the polar angle and ϕ the azimuthal one. (c) Schematic of the system consisting of two magnetic layers of thickness t_p and t_q, separated by a nonmagnetic spacer of thickness δ, supporting symmetric and antisymmetric oscillations under radio-frequency excitation.

role in determining the symmetry and dispersion of the heterostructure eigenmodes. Developing a compact analytical framework for dipolar-coupled systems is therefore essential for identifying the physical mechanisms governing the formation of collective spin-wave modes.

In contrast to laterally coupled waveguides (see Fig. 1), vertically coupled magnetic/nonmagnetic/magnetic (M/NM/M) waveguides can exhibit a $k \neq 0$ point where the coupling length may diverge, signaling a transition to an effectively uncoupled regime. This leads to coupling lengths that can vary potentially from infinite distances to sub-μm, thus paving the way to a rich variety of tunable-purpose devices, such as power splitters and 3D power transfer architectures [29,30].

In this work, we introduce an analytical model for spin waves in vertically coupled magnetic layers separated by a nonmagnetic spacer that suppresses direct exchange interaction. The model exploits a Fourier-space approach, starting from the linearized Landau-Lifshitz equation, and extends formalisms previously developed for planarly coupled waveguides [28,31]. By expressing the problem in terms of a tensorial operator that incorporates exchange, anisotropy, and both self and mutual dipolar interactions, we obtain a compact eigenvalue formulation that naturally yields symmetric and antisymmetric collective modes without invoking *ad hoc* splitting assumptions. The model is general to arbitrary relative orientations between the spin-wave wave vector and the equilibrium magnetization direction. We apply the formalism to recently investigated vertically stacked heterostructures and benchmark the analytical results against micromagnetic simulations.

II. FOURIER-SPACE APPROACH

A. Hypotheses and validity of the model

The model relies on four main approximations. First, we consider heterostructures that are uniformly magnetized, thereby excluding complex micromagnetic configurations such as multidomain states or noncollinear textures. Second, the magnetization profile along the out-of-plane direction is assumed to be uniform across the thickness of each layer, thus restricting the analysis to magnetic thin films, particularly concentrating on the fundamental volume mode ($n_z = 0$). This assumption also limits the validity of the model for Damon-Eshbach configuration to the dipolar region of the spectrum, i.e., where the condition $kt \ll 1$ can be satisfied [20].

Third, total pinning boundary conditions are assumed at the lateral edges [28]. In particular, in this study, we focus on the fundamental even width mode ($n_y = 0$) accounting for $m(y) = \cos\left(\frac{\pi}{w} y\right)$. This framework may be generalized to higher-order even and odd modes by adjusting the width profile and pinning conditions accordingly [32–34].

Finally, magnetic damping is not included in the present discussion. These four assumptions enable an analytical evaluation of the demagnetizing tensor in Fourier space and lead to a compact eigenvalue formulation for the coupled spin-wave modes. As a consequence, the model does not capture phenomena associated with nonuniform thickness profiles, boundary pinning effects, or partially saturated magnetic states. In particular, deviations from full agreement with micromagnetic simulations are expected at increasing wave vectors, where thickness-mode hybridization and nonuniform magnetization profiles become progressively more relevant.

B. Dipolarly coupled waveguides

The magnetization vector is defined within the small-signal approximation as

$$\vec{M}(\vec{r},t) = M_s\vec{\mu} + \vec{m}(\vec{r},t), \qquad \|\vec{m}(\vec{r},t)\| \ll M_s, \tag{1}$$

where $\vec{\mu}$ is the unit vector along the equilibrium magnetization direction, M_s is the saturation magnetization, and $\vec{m}(\vec{r},t) = (m_x, m_y, m_z)$ is the space- and time-dependent dynamic component describing the magnetization precession in the linear regime.

By substituting Eq. (1) into the Landau-Lifshitz-Gilbert equation, neglecting the damping term, and linearizing the resulting expression (see Supplemental Material S1 [70]), a Fourier-space representation [20] for spin waves propagating along the x direction is obtained,

$$-\mathrm{i}\,\omega_{k_x}^{(p)}\hat{\mathbf{I}}\,\vec{m}_{k_x}^{(p)} = \vec{\mu}\times\sum_q \hat{\mathbf{\Omega}}_{k_x}^{(pq)}\vec{m}_{k_x}^{(q)}, \tag{2}$$

where $p, q \in \{1,2\}$ label the magnetic layers, $\hat{\mathbf{I}}$ is the identity matrix, k_x is the wave vector along the propagation direction, and $\hat{\mathbf{\Omega}}_{k_x}^{(pq)}$ is a tensor operator incorporating exchange, dipolar, and uniaxial anisotropy contributions. Solving this equation allows us to write the associated eigenvalue problem of the system in the frequency domain.

The general form of the operator $\hat{\mathbf{\Omega}}_{k_x}^{(pq)}$ reads

$$\begin{aligned}\hat{\mathbf{\Omega}}_{k_x}^{(pq)} = {} & \gamma[B^{(p)} + \mu_0 M_s^{(p)}(\lambda_{\mathrm{ex}}^{(p)})^2(k_x^2+\kappa^2)]\delta_{pq}\hat{\mathbf{I}} \\ & - \omega_M^{(p)}\frac{2K^{(p)}}{\mu_0(M_s^{(p)})^2}(\vec{u}^{\,(p)}\otimes\vec{u}^{\,(p)})\delta_{pq} \\ & + \omega_M^{(q)}\hat{\mathbf{F}}_{k_x}^{(pq)}(d_{pq}),\end{aligned} \tag{3}$$

where γ is the gyromagnetic ratio and μ_0 is the vacuum permeability. The quantity $B^{(p)}$ denotes the static internal magnetic field of layer p, while the exchange length is defined as $\lambda_{\mathrm{ex}} = \sqrt{2A/(\mu_0 M_s^2)}$. Here $K^{(p)}$ and $\vec{u}^{\,(p)}$ are the anisotropy constant and anisotropy axis of layer p, respectively, and d_{pq} is the distance between the centers of the magnetic layers along the thickness direction. The contribution of the transverse wave vector is accounted for by $\kappa = \pi/w$, while $\omega_M = \gamma\mu_0 M_s$ is the zero-field Larmor frequency. The internal field $B^{(p)}$ [35] can be written explicitly as

$$\begin{aligned}B^{(p)} = {} & \vec{B}_a\cdot\vec{\mu} - \mu_0 M_s^{(p)}\vec{\mu}\cdot\left[\hat{\mathbf{F}}_{k_x=0}^{(pp)}(0) + \frac{M_s^{(q)}}{M_s^{(p)}}\hat{\mathbf{F}}_{k_x=0}^{(pq)}(d_{pq})\right]\vec{\mu} \\ & + \vec{\mu}\cdot\frac{2K^{(p)}}{M_s^{(p)}}(\vec{u}^{\,(p)}\otimes\vec{u}^{\,(p)})\vec{\mu},\end{aligned} \tag{4}$$

where $\vec{B}_a$ denotes the external magnetic field, $\hat{\mathbf{F}}_{k_x=0}^{(pp)}$ is the static self-demagnetizing tensor of the layer p, and $\hat{\mathbf{F}}_{k_x=0}^{(pq)}$ accounts for the correction arising from the embedding layer p within the heterostructure. The tensor $\hat{\mathbf{F}}_{k_x}^{(pq)}$ describes the dipolar interaction in reciprocal space, including self- and mutual coupling between the layers. Following Wang *et al.* [28], we exploit the Fourier-space approach developed by Beleggia *et al.* [36] to compute the dipolar field components of the coupled system. The dipolar tensor elements are given by

$$(\hat{\mathbf{F}}_{k_x}^{(pq)})_{ij} = \frac{1}{2\pi}\int_{-\infty}^{+\infty}(\hat{\mathbf{N}}_k^{(pq)})_{ij}\mathrm{d}k_y, \qquad i,j = x,y,z, \tag{5}$$

$$\hat{\mathbf{N}}_k^{(pq)} = \frac{|\sigma_k|^2}{\tilde{w}}\begin{pmatrix} \frac{k_x^2}{k^2}\Delta_{pq} & \frac{k_xk_y}{k^2}\Delta_{pq} & \mathrm{i}\frac{k_x}{k}\tilde{\Delta}_{pq}\,\mathrm{sign}(z_p-z_q) \\ \frac{k_xk_y}{k^2}\Delta_{pq} & \frac{k_y^2}{k^2}\Delta_{pq} & i\frac{k_y}{k}\tilde{\Delta}_{pq}\mathrm{sign}(z_p-z_q) \\ \mathrm{i}\frac{k_x}{k}\tilde{\Delta}_{pq}\,\mathrm{sign}(z_p-z_q) & i\frac{k_y}{k}\tilde{\Delta}_{pq}\mathrm{sign}(z_p-z_q) & \delta_{pq}-\Delta_{pq}\end{pmatrix}, \tag{6}$$

with auxiliary functions,

$$\Delta_{pq} = \tilde{f}(k, t_p, t_q, \delta) + [f(kt_p) - \tilde{f}(k, t_p, t_q, \delta)]\delta_{pq},$$
$$\tilde{\Delta}_{pq} = \tilde{f}(k, t_p, t_q, \delta)(1 - \delta_{pq}),$$
$$f(kt_p) = 1 - \frac{1 - e^{-kt_p}}{kt_p},$$
$$\tilde{f}(k, t_p, t_q, \delta) = \frac{(1 - e^{-kt_p})(1 - e^{-kt_q})}{2kt_p} e^{-k\delta},$$

where $k^2 = k_x^2 + k_y^2$, δ_{pq} is the Kronecker delta, t_q indicates the thickness of layer q, z_p and z_q denote the z positions of the centers of the two magnetic layers, σ_k is the Fourier transform of the transverse spin-wave profile, and $\tilde{w}$ is the normalization constant associated with the transverse mode $m(y)$ [28], and $\hat{\mathbf{N}}_k^{(pq)}$ is the magnetometric tensor [31] (the main steps of the derivation of the magnetometric tensor are reported in Supplemental Material S2 [70]).

In order to solve Eq. (2), it is possible to note that $\vec{\mu} \times \vec{v}$ (where $\vec{v}$ is a generic vector here) can be expressed in matrix form as

$$\vec{\mu} \times \vec{v} = \hat{\mu}\, \vec{v}, \qquad \hat{\mu} = \begin{pmatrix} 0 & -\mu_z & \mu_y \\ \mu_z & 0 & -\mu_x \\ -\mu_y & \mu_x & 0 \end{pmatrix}. \tag{7}$$

Equation (2) can thus be written for layers $p = 1, 2$ expressed as

$$\begin{cases} -i\omega_{k_x}^{(1)} \hat{\mathbf{I}}\, \vec{m}_{k_x}^{(1)} = \hat{\mu}\left(\hat{\mathbf{\Omega}}_{k_x}^{(11)} \vec{m}_{k_x}^{(1)} + \hat{\mathbf{\Omega}}_{k_x}^{(12)} \vec{m}_{k_x}^{(2)}\right) \\ -i\omega_{k_x}^{(2)} \hat{\mathbf{I}}\, \vec{m}_{k_x}^{(2)} = \hat{\mu}\left(\hat{\mathbf{\Omega}}_{k_x}^{(21)} \vec{m}_{k_x}^{(1)} + \hat{\mathbf{\Omega}}_{k_x}^{(22)} \vec{m}_{k_x}^{(2)}\right) \end{cases} \tag{8}$$

with $\vec{m}_{k_x} = (m_x, m_y, m_z) \in \mathbb{C}^3$. This allows us to reformulate the mathematical equations framework in an explicit eigenvalue problem:

$$-i\omega\, \hat{\mathbf{m}} = \hat{\mu}_C\, \hat{\Omega}_C\, \hat{\mathbf{m}}, \tag{9}$$

with $\mathbf{m}_{k_x} \in \mathbb{C}^6$ referring to the three spatial components of the magnetization in layers p and q, while $\hat{\mu}_C$ denotes the skew-symmetric matrix unveiling the coupling mechanism. This can be directly appreciated from the explicit tensor formalism below:

$$-i\begin{pmatrix} \hat{\boldsymbol{\omega}} & 0 \\ 0 & \hat{\boldsymbol{\omega}} \end{pmatrix}\begin{pmatrix} \vec{m}^{(1)} \\ \vec{m}^{(2)} \end{pmatrix} = \begin{pmatrix} \hat{\mu} & 0 \\ 0 & \hat{\mu} \end{pmatrix}\begin{pmatrix} \hat{\mathbf{\Omega}}^{(11)} & \hat{\mathbf{\Omega}}^{(12)} \\ \hat{\mathbf{\Omega}}^{(21)} & \hat{\mathbf{\Omega}}^{(22)} \end{pmatrix}\begin{pmatrix} \vec{m}^{(1)} \\ \vec{m}^{(2)} \end{pmatrix}, \tag{10}$$

with $\hat{\boldsymbol{\omega}} = \omega \hat{\mathbf{I}}_3$, and indices k_x have been neglected to simplify the notation.

This formulation enables a direct evaluation of the eigenmodes and dispersion relations in vertically coupled magnetic systems, where symmetric and antisymmetric spin-wave modes emerge from the dynamic dipolar interaction encoded in the off-diagonal tensors $\hat{\mathbf{\Omega}}^{(12)}$ and $\hat{\mathbf{\Omega}}^{(21)}$.

Within this framework, the associated eigenvalue problem can be solved, allowing direct access to the spin-wave dispersion relations and the corresponding dynamic magnetization profiles, along the propagation direction ($\hat{\mathbf{x}}$) for each layer. Expressing the equilibrium magnetization direction in spherical coordinates as $\vec{\mu} = (\sin\theta\cos\phi, \sin\theta\sin\phi, \cos\theta)$ enables a unified treatment of arbitrary orientations of the applied magnetic field with respect to the propagation direction $\hat{x}$, under the full-saturation approximation. The substitution of $\vec{\mu}$ into the skew-symmetric matrix $\hat{\mu}$ in Eq. (10) then allows the direct numerical evaluation of the eigenvalue problem.

Within this formalism, the model can be generalized to account for arbitrary relative orientations between the wave vector and the external magnetic field, as well as different layer thicknesses, saturation magnetizations, exchange constants, and anisotropy strengths and directions. The resulting eigenvalue problem can be efficiently solved using standard numerical approaches.

C. Homogeneous saturation magnetization in the absence of anisotropy

To extract the essential physical features of dipolarly coupled systems, we focus the analysis on two identical magnetic layers separated by a nonmagnetic spacer, neglecting magnetic anisotropies (Fig. 2). For these cases, it is possible to derive a closed and compact analytical formulation that highlights the role of dynamic dipolar coupling.

The diagonal blocks of the interaction tensor satisfy $\hat{\mathbf{\Omega}}^{(11)} = \hat{\mathbf{\Omega}}^{(22)}$, while the mutual interaction blocks obey $\hat{\mathbf{\Omega}}^{(12)} \neq \hat{\mathbf{\Omega}}^{(21)}$. This asymmetry originates directly from the opposite signs of the off-diagonal demagnetizing tensor components $\hat{N}_{k,xz}^{(pq)}$ and $\hat{N}_{k,xz}^{(qp)}$. The physical origin of this behavior lies in the layered geometry: the presence of an upper magnetic layer introduces a directional dependence in the dipolar interaction that is absent in laterally coupled systems [28], where the dipolar tensor remains symmetric, i.e., $\hat{\mathbf{\Omega}}^{(pq)} = \hat{\mathbf{\Omega}}^{(qp)}$.

In vertically coupled heterostructures, the relative displacement along the out-of-plane direction introduces a nontrivial phase factor in the mutual dipolar interaction. In particular, this results in a π-phase shift between the antidiagonal components of the interaction tensor $\hat{\Omega}_c$. This distinction can be formally understood by examining the construction of the diagonal and off-diagonal tensor blocks. The diagonal terms $\hat{\mathbf{\Omega}}^{(pp)}$ arise from integration over the thickness of each individual waveguide and therefore describe intralayer interactions, remaining formally analogous to the lateral case. In contrast, the mutual terms $\hat{\mathbf{\Omega}}^{(pq)}$ $(p \neq q)$ involve integration across the full

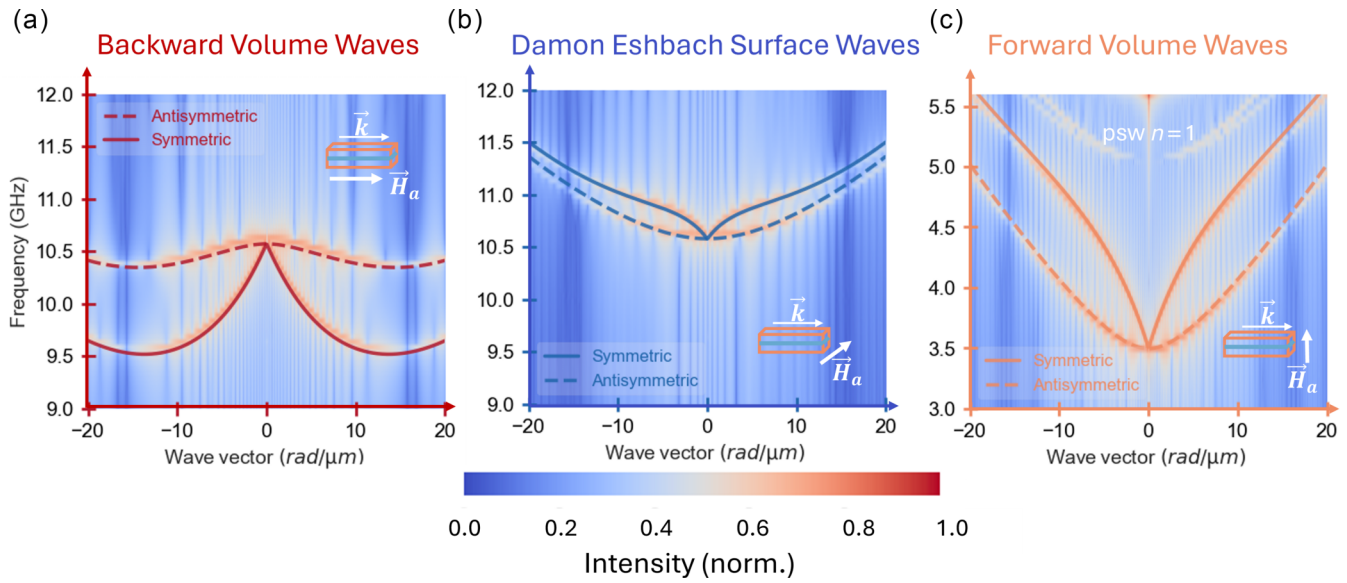


FIG. 2. (a)–(c) Comparison between micromagnetic simulations performed using OOMMF (see Supplemental Material S3 [70]) and the analytical model for the backward-volume, Damon-Eshbach, and forward-volume configurations, respectively, in the absence of magnetic anisotropy, for YIG100 nm/NM4 nm/YIG100 nm thin film heterostructure with a 200×200 μm simulation size, with $\mu_0 H_a = 300$ mT.

heterostructure thickness and encode interlayer dipolar coupling. This structural asymmetry is explicitly captured by the auxiliary functions Δ_{pq} and $\tilde{\Delta}_{pq}$, which govern self- and mutual-layer contributions, respectively, and the sign function $\mathrm{sign}(z_p - z_q)$ present in xz and yz terms of $\hat{\mathbf{N}}_k^{(pq)}$.

Despite the lack of symmetry between the mutual interaction tensors, the mathematical properties of the integrals defining the demagnetizing tensor allow a partial simplification of the problem. In particular, it leads to:

(i) $F^{(12)}_{k_x,xy} = F^{(21)}_{k_x,xy} = 0$,

(ii) $F^{(12)}_{k_x,xz} = -F^{(21)}_{k_x,xz}$, with $F^{(12)}_{k_x,xz}, F^{(21)}_{k_x,xz} \in \mathbb{I}\mathrm{m}$,

(iii) $F^{(12)}_{k_x,ii} = F^{(21)}_{k_x,ii}$, with $F^{(12)}_{k_x,ii}, F^{(21)}_{k_x,ii} \in \mathbb{R}$,

where $i = x, y, z$. This approach enables a unified treatment of spin-wave dispersion according to the relative angle between the magnetization and the applied external magnetic field, leading to the general mathematical form:

$$\omega_{s,as} = \sqrt{\Omega_0 \pm \omega_M \sqrt{\Omega'}}. \tag{11}$$

In each case, the unit vector $\vec{\mu}$ defines the equilibrium magnetization direction, and its substitution into the skew-symmetric matrix $\hat{\mu}_C$ allows the derivation of the respective analytical expressions. Here, we explicitly state the analytical forms for the three main dipolar configurations:

(i) *Backward-volume (BV) waves* ($\vec{k} \| \vec{\mu}$, coplanar):

$$\begin{aligned} \Omega_0 &= \Omega_{yy}\Omega_{zz} + \omega_M^2 F^{(12)}_{yy} F^{(12)}_{zz}, \\ \Omega' &= \left(\Omega_{yy} F^{(12)}_{zz} + \Omega_{zz} F^{(12)}_{yy}\right)^2. \end{aligned} \tag{12}$$

(ii) *Damon-Eshbach (DE) surface waves* ($\vec{k} \perp \vec{\mu}$, coplanar):

$$\begin{aligned} \Omega_0 &= \Omega_{xx}\Omega_{zz} + \omega_M^2 F^{(12)}_{xx} F^{(12)}_{zz} + \omega_M^2 (F^{(12)}_{xz})^2, \\ \Omega' &= \left(\Omega_{zz} F^{(12)}_{xx} + \Omega_{xx} F^{(12)}_{zz}\right)^2 \\ &\quad + 4\omega_M^2 F^{(12)}_{xx} F^{(12)}_{zz} \left(F^{(12)}_{xz}\right)^2. \end{aligned} \tag{13}$$

(iii) *Forward-volume (FV) waves* (noncoplanar $\vec{k}$ and $\vec{\mu}$):

$$\begin{aligned} \Omega_0 &= \Omega_{xx}\Omega_{yy} + \omega_M^2 F^{(12)}_{xx} F^{(12)}_{yy} \\ &\quad + \omega_M^2 \left(F^{(12)}_{xy}\right)^2 - \omega_M^2 F^2_{xy}, \\ \Omega' &= \left(\Omega_{yy} F^{(12)}_{xx} + \Omega_{xx} F^{(12)}_{yy}\right)^2 \\ &\quad + 4\omega_M^2 F^{(12)}_{xx} F^{(12)}_{yy} \left(F^{(12)}_{xy}\right)^2 - 4\omega_M^2 F^2_{xy} \left(F^{(12)}_{xy}\right)^2. \end{aligned} \tag{14}$$

Upon numerical evaluation of the integrals defining the tensor elements $(\hat{\boldsymbol{F}}^{(pq)}_{k_x})_{ij}$, the corresponding dispersion relations can be obtained. The resulting spectra, shown in Figs. 2(a)–2(c), display good agreement with Object Oriented MicroMagnetic Framework (OOMMF) micromagnetic simulations [37] and the TetraX [38,39] packages. Simulation details are provided in Supplemental Material S3 [70]. From the eigenvalue solution, the associated eigenvectors can be obtained, allowing the reconstruction of the spatial profiles of the dynamic magnetization, as illustrated in Figs. 3(b)–3(d). When

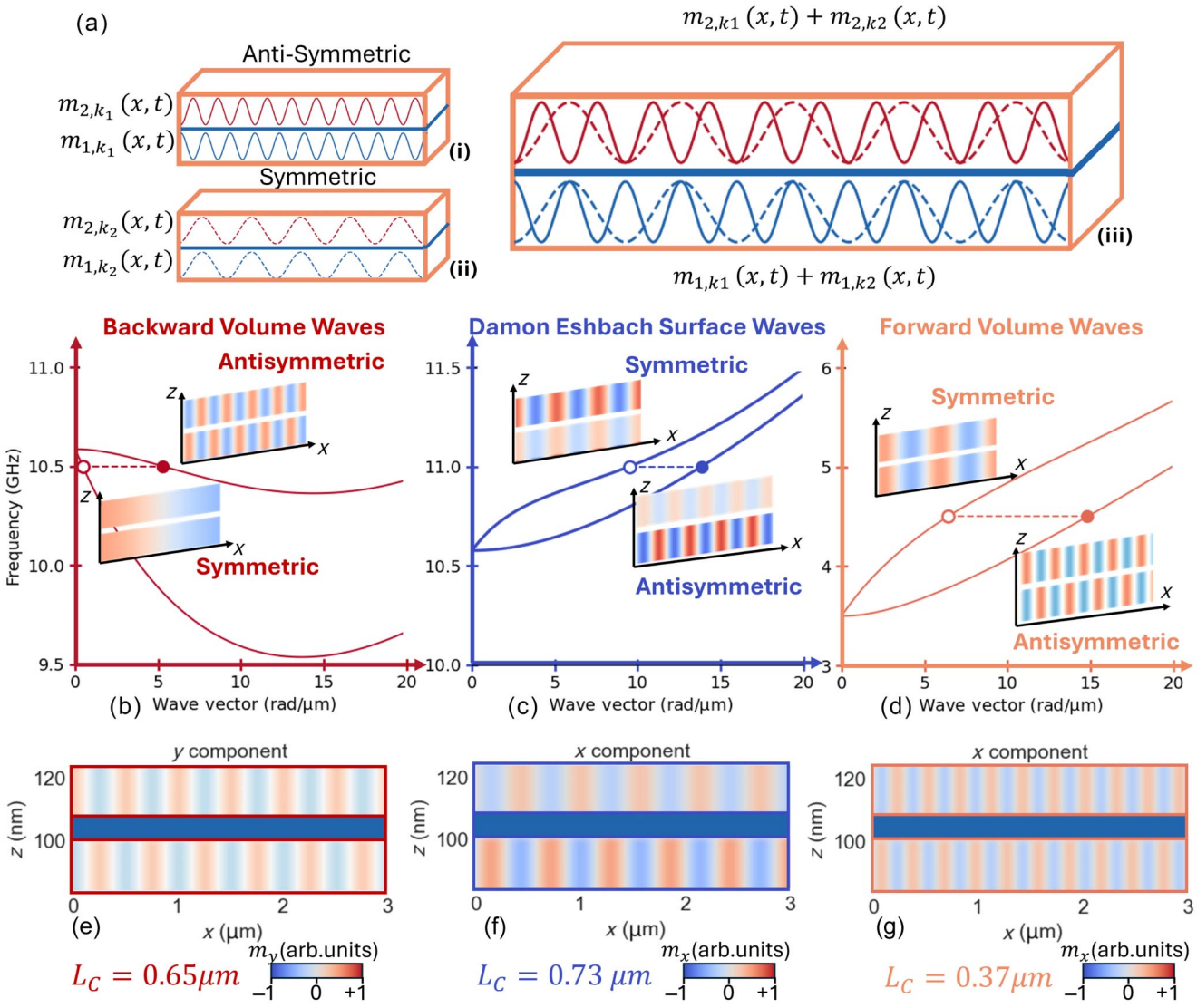


FIG. 3. (a) Qualitative sketch of the symmetric and antisymmetric spin-wave profiles (i), (ii) and their collective behavior due to interference at fixed frequency (iii). (b)–(d) Dispersion relations in the positive-wave vector region for a YIG/NM/YIG heterostructure (micromagnetic parameters of YIG are listed in Table I), with $t = 100$ nm, $\delta = 4$ nm, $w = 200$ μm and an applied external field $\mu_0 H_a = 300$ mT, highlighting the symmetric and antisymmetric character of the oscillating magnetization at the resonant frequency for each spin-wave configuration. Insets show the associated spin-wave mode normalized profile amplitude $m^{p,q}(x)$, with p and q the top and bottom layers. (e)–(g) Normalized oscillating spatial intensity $[\cos(\Delta k_x x + \Delta\phi_k)]$ of the dynamic magnetization resulting from the coexistence of the two wave vectors selected at a fixed excitation frequency [as indicated in (b)–(d) dashed lines], shown for the BV, DE, and FV configurations, respectively, together with the associated coupling length L_C.

the system is driven at a fixed frequency, the excitation intersects both the symmetric and antisymmetric branches at the wave vectors k_s and k_{as}. The real space magnetization profile along the propagation direction for each of these modes is expressed as

$$m(x,\omega_i) = \frac{\left|m_{k_i}^{(p)}\right|}{\left|m_{k_i}^{(p)}\right| + \left|m_{k_i}^{(q)}\right|} \cos\left(k_i x + \phi_{k_i} - \omega_i t\right), \quad (15)$$

with $i = s, as$ and $p, q = 1, 2$.

The resulting superposition of symmetric and antisymmetric modes gives rise to the spatial modulation of the spin-wave intensity across the heterostructure. For a given magnetic layer p and component i, the specific dynamic magnetization component can be written explicitly as

$$\tilde{m}(x,t) = 2|m_{k_s}| \cos\left(k_s x + \phi_{k_s} - \omega t\right) + 2|m_{k_{as}}| \cos\left(k_{as} x + \phi_{k_{as}} - \omega t\right), \quad (16)$$

where $|m_{k_s}|$, $|m_{k_{as}}|$ and ϕ_{k_s}, $\phi_{k_{as}}$ are the moduli [weighted over the heterostructure as expressed in Eq. (15)] and phases of the respective eigenvectors. This can lead to an associated time-averaged intensity $I(x) \propto \langle \tilde{m}^2(x,t)\rangle_t$:

$$I(x) \propto 2|m_{k_s}|^2 + 2|m_{k_{as}}|^2 + 4|m_{k_s}||m_{k_{as}}|\cos(\Delta k_x x + \Delta\phi_k), \quad (17)$$

showing that the resulting interference pattern is sinusoidally distributed along the propagation direction, periodically concentrating the energy into one or the other layer, as depicted in Figs. 3(e)–3(g). For each wave vector k_x, the dispersion relation exhibits both higher and lower frequency branches, corresponding to collective symmetric and antisymmetric excitations of the heterostructure, as can be appreciated from the reported spatial profiles $m^{p,q}(x)$ in Fig. 3.

Even within this simplified setting, we emphasize that the analytical model is built upon the linearization of the Landau-Lifshitz-Gilbert equation, where the two magnetic layers are initially treated as independent subsystems, as reflected in the structure of the tensor $\hat{\mathbf{\Omega}}_{k_x}^{(pq)}$ on the right-hand side of Eq. (10).

The dynamic coupling between the layers emerges only through the careful evaluation of the coupled terms. In fact recasting the right-hand side of Eq. (2) with the auxiliary skew matrix properly captures the complex dipolar landscape of the structure. It describes both the behavior of the single layer as an isolated system, and the energetic terms from being embedded in the heterostructure, thus preventing a simple linear Bloch-type picture of the form $\Omega_0 \pm \Omega'$. This highlights the intrinsically nontrivial nature of the modes in dipolarly coupled systems, where the eigenfrequencies result from the full tensorial structure of the mutual interaction rather than from a perturbative splitting of uncoupled modes. Figures 3(b)–3(d) schematically illustrates the spatial profiles associated with the symmetric and antisymmetric modes. The two precession states exhibit the same resonant frequency with distinct spatial modulation. In principle, this can be exploited to induce controlled interference effects within the heterostructure through appropriate design of the radio-frequency transducers [40,41].

III. SIMPLIFIED PERTURBATIVE APPROACH

As discussed above, a full analytical determination of the eigenvalues and eigenvectors of the system requires solving the complete coupled spin-wave eigenproblem,

$$\hat{\mu}_C \hat{\mathbf{\Omega}}_C \mathbf{m} = -\mathrm{i}\omega\,\mathbf{m}, \quad (18)$$

where the intrinsic coupling between the layers is encoded in the tensor $\hat{\mathbf{\Omega}}$. While this formulation captures the physics exactly, its complexity motivates the introduction of a simplified perturbative approach, which nevertheless provides insight into the nature and energy of the collective modes.

Within this simplified model we can think to separate the eigenvalues of the uncoupled layers from the coupling mechanism. Let us introduce the matrix Θ^0, accounting for the intralayer terms, and Θ' for the interlayer terms.

We may rewrite Eq. (18) as

$$(\Theta^0 + \lambda\Theta')(\phi + \lambda\phi') = -\mathrm{i}(\omega_0 + \lambda\omega')(\phi + \lambda\phi'), \quad (19)$$

where we write $\mathbf{m}$ as the sum of an unperturbed eigenvector ϕ plus a perturbative correction ϕ'.

Noting that in the BV, DE, and FV configurations, the full operator $\hat{\mu}_C\hat{\mathbf{\Omega}}_C$ can always be reduced to a four-dimensional subspace, the eigenproblem can be written as

$$\left[\begin{pmatrix}\Theta^0_{pp} & 0\\ 0 & \Theta^0_{qq}\end{pmatrix} + \begin{pmatrix}0 & \Theta'_{pq}\\ \Theta'_{qp} & 0\end{pmatrix}\right]\begin{pmatrix}c_1\\ c_2\end{pmatrix} = -\mathrm{i}\omega\begin{pmatrix}c_1\\ c_2\end{pmatrix}. \quad (20)$$

Since the problem is non-Hermitian, left and right eigenvectors must be introduced, satisfying the biorthonormality condition $\langle\phi_i^L|\phi_j^R\rangle = \delta_{ij}$ [42,43].

The perturbative eigenproblem then takes the generalized form

$$\begin{pmatrix}\langle\phi_1^L|\Theta'|\phi_1^R\rangle & \langle\phi_1^L|\Theta'|\phi_2^R\rangle\\ \langle\phi_2^L|\Theta'|\phi_1^R\rangle & \langle\phi_2^L|\Theta'|\phi_2^R\rangle\end{pmatrix}\begin{pmatrix}\alpha\\ \beta\end{pmatrix} = -\mathrm{i}\omega'\begin{pmatrix}\alpha\\ \beta\end{pmatrix}. \quad (21)$$

This system yields two degenerate unperturbed solutions at frequency ω_0, associated with left and right eigenvectors $\phi_{1,2}^{L,R}$. A compact expression, valid for all three configurations in an infinite film, is obtained by choosing $(i,j) = (y,z)$ in the BV case, (x,z) in the DE case, and (x,y) in the FV case:

$$\phi_1^L = \frac{1}{\sqrt{2}}\left(\pm\mathrm{i}\frac{\Omega_{ii}}{\omega_0}, 1, 0, 0\right), \qquad \phi_1^R = \frac{1}{\sqrt{2}}\begin{pmatrix}\mp\mathrm{i}\frac{\Omega_{jj}}{\omega_0}\\ 1\\ 0\\ 0\end{pmatrix},$$

$$\phi_2^L = \frac{1}{\sqrt{2}}\left(0, 0, \pm\mathrm{i}\frac{\Omega_{ii}}{\omega_0}, 1\right), \qquad \phi_2^R = \frac{1}{\sqrt{2}}\begin{pmatrix}0\\ 0\\ \mp\mathrm{i}\frac{\Omega_{jj}}{\omega_0}\\ 1\end{pmatrix}. \quad (22)$$

Projecting the perturbation onto the degenerate subspace yields

$$\Theta' = \begin{pmatrix} 0 & -\frac{i\omega_M}{2}\Delta \\ -\frac{i\omega_M}{2}\Delta & 0 \end{pmatrix}, \qquad \Delta = \frac{\Omega_{ii}F_{jj} + \Omega_{jj}F_{ii}}{\omega_0}, \tag{23}$$

which allows the calculation of the frequency correction ω' and the associated eigenvectors $\phi'_\pm = \alpha_\pm\phi_1 + \beta_\pm\phi_2$:

$$\omega' = \pm\frac{\omega_M}{2}|\Delta|, \qquad \phi'_+ = \begin{pmatrix} \frac{\Delta}{|\Delta|} \\ 1 \end{pmatrix}, \qquad \phi'_- = \begin{pmatrix} -\frac{\Delta}{|\Delta|} \\ 1 \end{pmatrix}. \tag{24}$$

These solutions represent the collective symmetric and antisymmetric oscillations of the two magnetic layers. Within this framework, it is possible to identify how the mode symmetry is associated with the, higher and lower, frequency branches at a given wave vector. Inspection of Fig. 4 reveals that the sign of Δ exhibits opposite behavior in the BV configuration compared with the DE and FV cases. As a consequence, the symmetric and antisymmetric modes belong to the lower and higher frequency branches, respectively, in the DE and FV configurations, while the opposite occurs in the BV configuration. This implies that, at a fixed excitation frequency, the symmetric mode is associated with the smaller wave vector and therefore with the larger wavelength, in the case of an infinite film. Within this simplified perturbative approach, the separation between the bands and its behavior in laterally confined cases can be directly evaluated and compared with the computed Ω' from Eqs. (12)–(14) (see Supplemental Material S4 [70]).

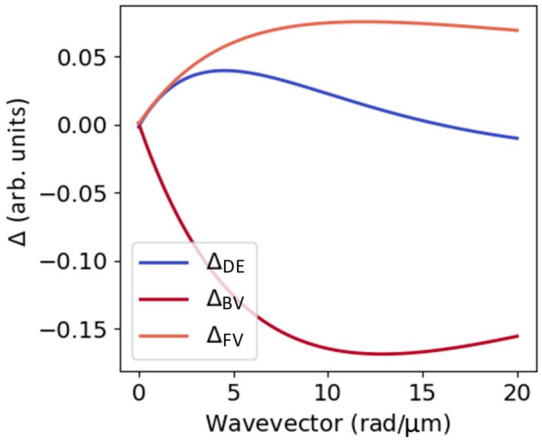


FIG. 4. Frequency correction, Δ, calculated from the simplified perturbative model for different spin-wave configurations in the case of YIG heterostructure (micromagnetic parameters in Table I with $w = 100$ μm, $t = 100$ nm, $\delta = 4$ nm, and $\mu_0 H_a = 300$ mT. Notably, the BV configuration exhibits an opposite trend compared with DE and FV, accounting for the distinct association of symmetric and antisymmetric modes with the two branches.

IV. MODEL EVALUATION

Having established the analytical framework, we now evaluate the predictive capabilities of the model and illustrate how appropriate choices of geometry and material parameters allow engineering of the spin-wave dispersion relations and the associated spin-wave modes. We begin by considering common representative magnonic materials: yttrium iron garnet (YIG), permalloy (NiFe), and cobalt iron boron (CoFeB), in BV and DE spin-wave configurations [27–29,44–47]. The corresponding material parameters and film thicknesses used in the calculations are summarized in Table I.

In Fig. 5, the resulting dispersion relations for the studied heterostructures are shown, including symmetric CoFeB, NiFe, and YIG bilayers, as well as their asymmetric combinations.

As expected, the ferromagnetic resonance (FMR, i.e., $k_x = 0$) coincides in the DE and BV configurations. In contrast, making the two layers from different materials leads to the opening of a gap at $k_x = 0$ with respect to the case of heterostructures composed of the same magnetic material [vertical arrows in Figs. 5(c) and 5(d)]. No dipolar coupling occurs for $k \to 0$, due to vanishing off-diagonal terms in Eq. (10), i.e., retrieving the expected distinct FMR of the two layers. Interestingly enough, in DE configuration, comparison between the NiFe/CoFeB and CoFeB/NiFe stacks reveals that reversing the material order provides an additional degree of freedom to control the propagation direction and group velocity of spin waves, as correctly captured by the presented model.

In general, when the two magnetic layers possess different micromagnetic parameters, a finite gap opens between the symmetric and antisymmetric branches. Equivalently, this behavior can be interpreted as the lifting of a degeneracy at $k_x = 0$, as will be discussed in more detail in Sec. IV A. The gap opening between two branches can be directly traced back to the micromagnetic contributions entering the definition of the internal fields, which modify the diagonal terms of the interaction tensor. This indicates that material doping, interface engineering, or growth-induced variations in magnetic parameters can be used to tune the dispersion relations and mode symmetry according to the desired functionality of the heterostructure.

In particular, in the DE configuration for nonequivalent layers, a pronounced nonreciprocal behavior emerges [48–50]. In contrast to the BV case, in the DE configuration the F_{xz} and F_{zx} terms enter explicitly into the eigenvalue formulation, thereby introducing a nonreciprocal correction. As will be further clarified in Sec. IV A, this behavior represents a general property of this micromagnetic configuration, namely that any micromagnetic asymmetry between the two layers is translated into a nonreciprocal spin-wave response.

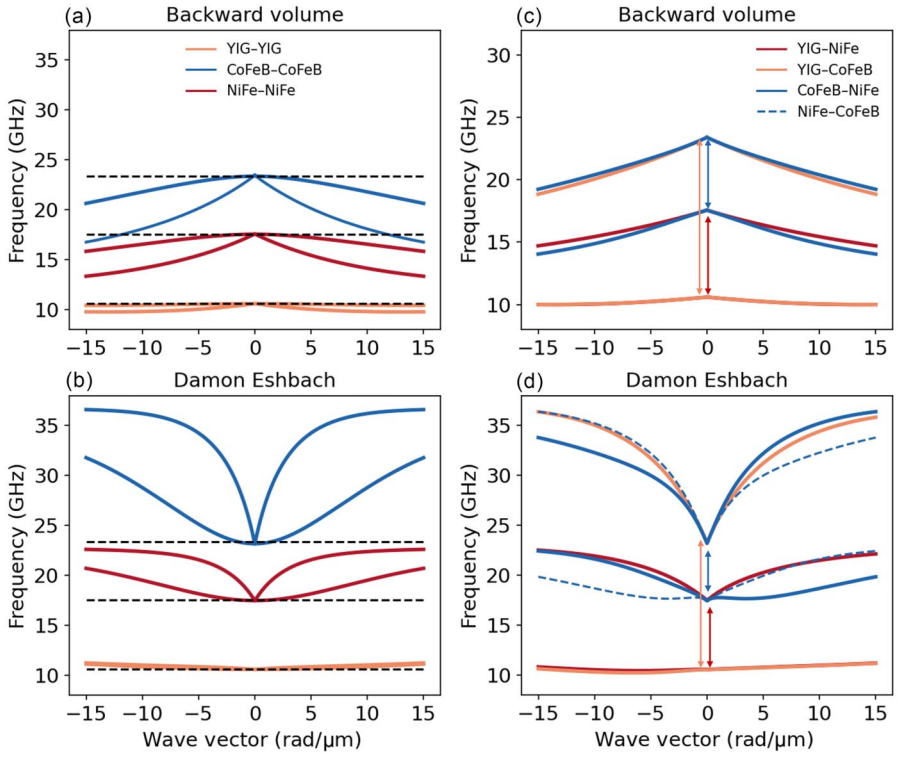


FIG. 5. Calculated spin-wave dispersion relations for an external applied field $\mu_0 H_a = 300$ mT in the backward-volume and Damon-Eshbach configurations for M/NM/M trilayers composed of the same magnetic material: YIG/NM/YIG, CoFeB/NM/CoFeB, and NiFe/NM/NiFe (a),(b). All structures have identical magnetic layer thicknesses $t_p = t_q = t = 80$ nm and a spacer thickness $\delta = 20$ nm. The dashed black lines indicate the coincident FMR frequencies of the two magnetic layers in the homogeneous case. (c),(d) Spin-wave dispersion relations in the BV and DE configurations, respectively, for trilayers containing different magnetic materials: YIG/NM/NiFe, YIG/NM/CoFeB, and NiFe/NM/CoFeB, as well as the inverted stacking order CoFeB/NM/NiFe. The layer thicknesses are $t_p = t_q = t = 80$ nm and $\delta = 20$ nm. These panels highlight the impact of material asymmetry on the separation (vertical arrows) between the spin-wave branches and on the emergence of nonreciprocal behavior in the DE configuration.

A. Dipolarly coupled iron garnets

Given the model's material agnosticism, we now focus our analysis on iron-garnet-based heterostructures. These materials offer a unique combination of low damping, tunable magnetization and anisotropy, while maintaining high epitaxial quality [51–57]. For instance, in pulsed-laser-deposited films, not only can the cation-site occupancy be tailored through chemical composition, but growth parameters such as substrate choice, deposition atmosphere, and temperature can be exploited to engineer strain and anisotropy [58,59]. Perpendicular magnetic anisotropy can be induced via magnetoelastic or magnetotaxial effects and tuned through lattice or thermal mismatch strain between the film and the substrate [60–62]. Moreover, an appropriate choice of the nonmagnetic spacer could allow the suppression of interfacial exchange coupling, while preserving the epitaxy, and then ensuring that the interaction between the magnetic layers is purely dipolar. From a modeling perspective, iron garnets therefore represent a nearly ideal material framework to explore the parameter variations presented in this work [62–68].

TABLE I. Micromagnetic parameters employed in the model evaluation [saturation magnetization (M_s), exchange stiffness (A)], and in the micromagnetic simulations (damping α).

Material	M_s (kA/m)	A (pJ/m)	α
YIG	140	4	1×10^{-4}
NiFe	800	10	5×10^{-3}
CoFeB	1600	15	1×10^{-3}

As a result, garnet-based heterostructures provide a clean and experimentally relevant testbed to assess the predictive power of the model and to explore how controlled layer asymmetry influences collective spin-wave dispersion and mode behavior [51,52,54,56]. We start by considering the simplified case of two identical YIG layers separated by a nonmagnetic spacer. In Figs. 6(a)–6(d), the impact of the YIG layer thickness and spacer thickness on the spin-wave dispersion is presented.

At a fixed spacer thickness δ, increasing the magnetic layer thickness leads to an increase in the group velocity. Conversely, for increasing spacer thickness, the band

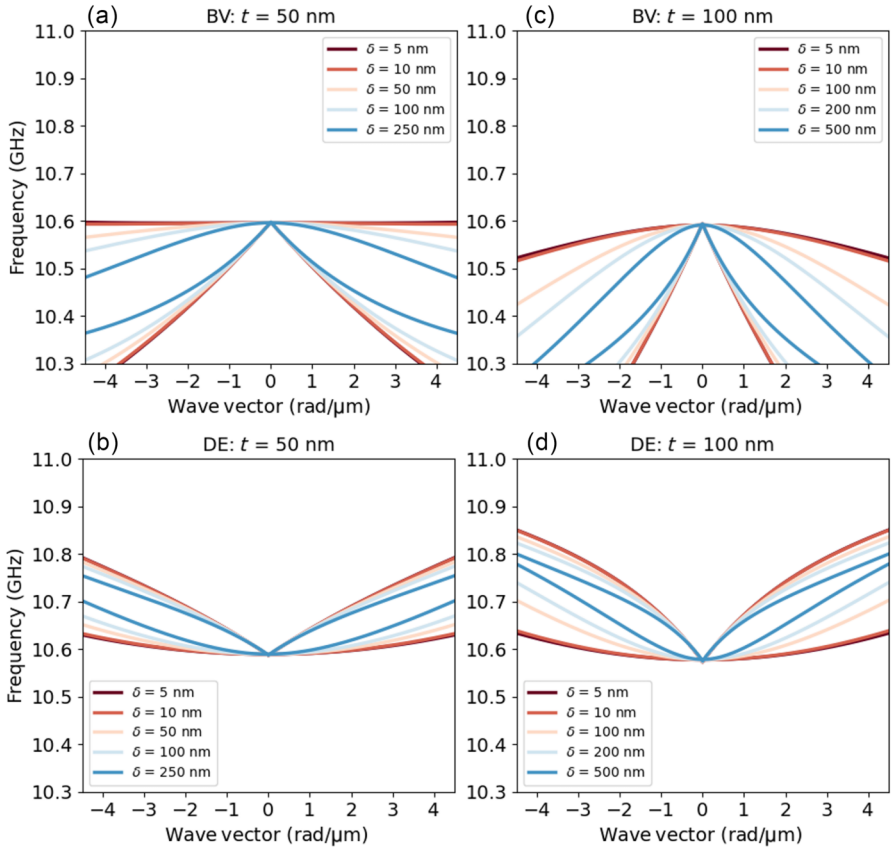


FIG. 6. (a),(b) Calculated spin-wave dispersion relations with an applied external field $\mu_0 H_a = 300$ mT for two identical infinite YIG layers with thickness $t = 50$ nm (micromagnetic parameters in Table I), separated by a nonmagnetic spacer of increasing thickness δ. (c),(d) Calculated spin-wave dispersion relations for two identical infinite YIG layers with thickness $t = 100$ nm (micromagnetic parameters in Table I), separated by a nonmagnetic spacer of increasing thickness δ. Increasing the spacer thickness progressively reduces the separation between the symmetric and antisymmetric branches, approaching the single-waveguide limit, consistent with the decay of dynamic dipolar coupling with interlayer distance.

separation progressively decreases, approaching the limiting case of a single, isolated layer.

In Figs. 7(a) and 7(d), we perform an equivalent analysis by varying the width of the YIG/NM/YIG stack, ranging from the infinite-film limit, where the FMR resonances of two identical layers are indistinguishable, to laterally confined waveguides. Specifically, in the Damon-Eshbach configuration, we observe a minimum frequency gap (anticrossing point) between the branches that increases as the waveguide width decreases and shifts toward larger wave vectors. Conversely, in the backward-volume configuration, the two branches exhibit an intersection point (crossing point), which also migrates toward larger wave vectors as the waveguide width decreases. It is significant to note that higher-order transverse modes, arising from the finite width of the waveguide, are neglected here. Despite this simplification, the model captures the essential physical trends.

While the dipolar interaction vanishes at $k = 0$, making the FMR frequencies of the two infinite equivalent magnetic layers truly degenerate, the behavior at $k \neq 0$ of the waveguide geometry warrants further discussion. In fact, the degeneracy with respect to an isolated magnetic waveguide is always lifted by nontrivial dipolar terms; however, in the backward-volume configuration, equivalent magnetic materials truly present a degenerate point (crossing). On the contrary, in the Damon-Eshbach configuration, it is always lifted. Specifically, as reported in Fig. 7, this behavior arises from the dependency of Ω' on $F_{zz}^{(12)}$ in both DE and BV configurations. Given that $F_{zz}^{(12)} \leq 0$ while $F_{xx}^{(12)}, F_{yy}^{(12)} \geq 0$, the terms $\Omega_{yy} F_{zz}^{(12)} + \Omega_{zz} F_{yy}^{(12)}$ in Eq. (12) and $\Omega_{xx} F_{zz}^{(12)} + \Omega_{zz} F_{xx}^{(12)}$ in Eq. (13) cross zero, a feature absent in the FV configuration, which does not depend on F_{zz}. This results in a local minimum of Ω' for both in-plane field configurations; this minimum manifests as an exact crossing in the BV case, whereas in the DE configuration, it is lifted by the term $4\omega_M^2 F_{xx}^{(12)} F_{zz}^{(12)} (F_{xz}^{(12)})^2$, which is null only at $k_x = 0$ [see Figs. 7(c), 7(f), and Supplemental Material S5 [70]]. Interestingly, the $F_{xz}^{(12)}$ term is responsible for the broken parity symmetry of $\hat{\mu}_C \hat{\Omega}_C$ in the DE configuration; this symmetry is also absent in heterostructures with

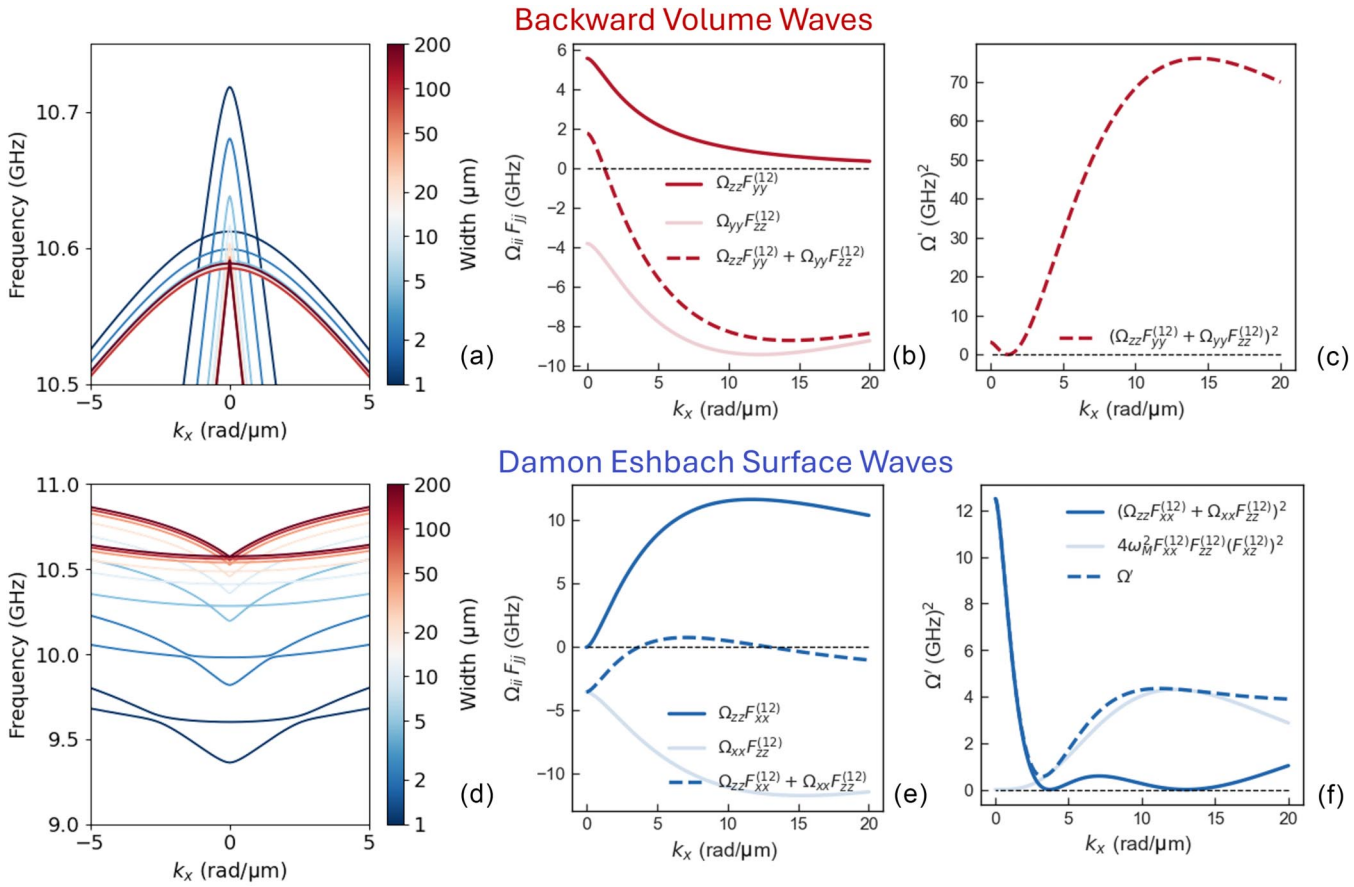


FIG. 7. (a) Calculated spin-wave dispersion relations in the BV configuration for two identical YIG layers of thickness $t = 100$ nm (micromagnetic parameters listed in Table I), separated by a nonmagnetic spacer of thickness $\delta = 4$ nm, for increasing lateral width w and an applied field $\mu_0 H_a = 300$ mT. (b) Individual terms entering the frequency correction Ω' in the BV configuration, for a lateral dimension $w = 1$ μm. The absolute minimum of Ω' is exactly zero because the negative sign of $F_{zz}^{(12)}$ makes the combination $\Omega_{zz}F_{yy}^{(12)} + \Omega_{yy}F_{zz}^{(12)}$ cross zero, which in turn makes Ω' truly vanish. (c) Frequency correction $\Omega' = (\Omega_{zz}F_{yy}^{(12)} + \Omega_{yy}F_{zz}^{(12)})^2$ evaluated for a lateral width $w = 1$ μm in the BV configuration, showing the exact zero discussed in the text. (d) Calculated spin-wave dispersion relations in the DE configuration for two identical YIG layers of thickness $t = 100$ nm (micromagnetic parameters listed in Table I), separated by a nonmagnetic spacer of thickness $\delta = 4$ nm, for increasing lateral width w and an applied field $\mu_0 H_a = 300$ mT. (e) Individual terms entering Ω' in the DE configuration, for a lateral dimension $w = 1$ μm. As in the BV case, the diagonal combination $\Omega_{zz}F_{xx}^{(12)} + \Omega_{xx}F_{zz}^{(12)}$ crosses zero because of the negative sign of $F_{zz}^{(12)}$; taken by itself, its square would vanish and would produce an exact crossing. (f) Full frequency correction $\Omega' = (\Omega_{zz}F_{xx}^{(12)} + \Omega_{xx}F_{zz}^{(12)})^2 + 4\omega_M^2 F_{xx}^{(12)}F_{zz}^{(12)}(F_{xz}^{(12)})^2$ evaluated for $w = 1$ μm in the DE configuration. Because $F_{xz}^{(12)}$ is purely imaginary, $(F_{xz}^{(12)})^2 < 0$; together with $F_{zz}^{(12)} \leq 0$ and $F_{xx}^{(12)} \geq 0$, the off-diagonal term $4\omega_M^2 F_{xx}^{(12)}F_{zz}^{(12)}(F_{xz}^{(12)})^2$ is positive. At the wave vector where the diagonal combination $\Omega_{zz}F_{xx}^{(12)} + \Omega_{xx}F_{zz}^{(12)}$ crosses zero this term is strictly positive, so Ω' never reaches zero and the two branches anticross rather than cross in the DE configuration.

different micromagnetic parameters in the two layers. In addition, the dispersion branches are shifted in opposite directions depending on the configuration: in the BV geometry, the bands are shifted upward, as shape anisotropy favors magnetization alignment parallel to the propagation direction, while in the DE geometry the dispersion is shifted downward, since shape anisotropy makes the y direction a hard axis.

We next consider the impact of layer asymmetry by introducing different saturation magnetizations M_s for the top and bottom layers at fixed width [27,47], as well as the effect of an interfacial magnetoelastic term. The latter can be modeled as an additional perpendicular magnetic anisotropy in the top layer. The corresponding results are shown in Fig. 8.

The saturation magnetization M_s has a pronounced impact on both the overall bandwidth of the dispersion relations and the resulting group velocities. In particular, lowering M_s of one layer leads to a systematic shift of the spin-wave branches toward lower frequencies and enhances the separation between the symmetric and antisymmetric modes at low k.

This analysis reveals the range of dispersion relations, gap opening and nonreciprocal behavior that can

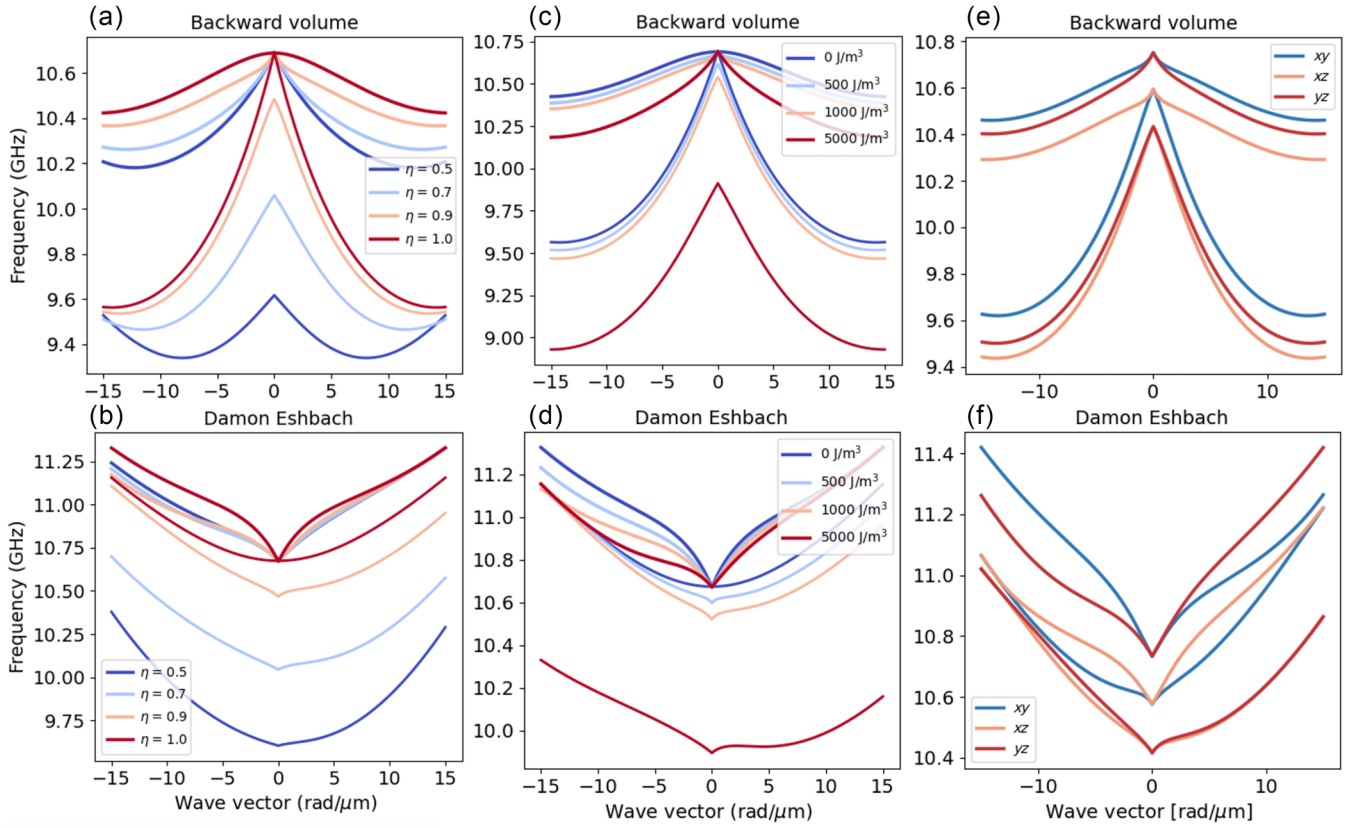


FIG. 8. (a),(b) Spin-wave dispersion relations at an external applied field $\mu_0 H_a = 300$ mT in the backward-volume and Damon-Eshbach configurations for two YIG layers of thickness $t_{\mathrm{YIG}} = 100$ nm, separated by a nonmagnetic spacer of thickness $\delta = 4$ nm, with different saturation magnetizations, where $M_{s,q} = \eta M_{s,p}$ and $\eta \leq 1$, in the absence of magnetic anisotropy. As the mismatch between the saturation magnetizations of the two layers increases, the separation between the symmetric and antisymmetric branches increases, with the lower branch shifting to lower frequencies. (c),(d) Spin-wave dispersion relations in the BV and DE configurations for two YIG layers with identical saturation magnetization, where the top layer hosts a perpendicular magnetic anisotropy modeled as a uniaxial anisotropy along $\mathbf{u} = (0, 0, 1)$. Results are shown for different values of the anisotropy constant K. The introduction of anisotropy produces an asymmetry between the layers, leading to an increased separation between the branches, reproducing the same qualitative trend observed in panels (a),(b). In the DE configuration, this anisotropy-induced asymmetry modifies the dispersion and the spatial distribution of the dynamic magnetization. (e),(f) Spin-wave dispersion relations in the BV and DE configurations for two YIG layers with identical saturation magnetization and an anisotropy constant $K = 1000$ J m^{-3}. The panels illustrate the effect of crossed anisotropy directions between the two layers. Specifically, configurations with the bottom layer anisotropy axis $\mathbf{u} = (1, 0, 0)$ and the top layer axis $\mathbf{u} = (0, 1, 0)$ (xy crossed anisotropy), as well as mixed in-plane and out-of-plane (x or yz) configurations with $\mathbf{u} = (1, 0, 0)$ or $(0, 1, 0)$ in the bottom layer and $\mathbf{u} = (0, 0, 1)$ in the top layer are considered.

be obtained by modifying the magnetic properties and geometry of the two layers [14]. In principle, the full anisotropy landscape of each garnet layer can be engineered. For example, Fig. 8 presents the effect of varying the anisotropy axis $\vec{u}_p$ of the layers to be orthogonal, altering the nonreciprocal response of the heterostructure [57]. These configurations highlight how anisotropic asymmetries between the layers modify the frequency separation between the symmetric and antisymmetric branches and can affect the dispersion reciprocity. From a mathematical standpoint, this behavior originates from the introduction of off-diagonal nonreciprocal terms proportional to K_u, independently of the micromagnetic configuration, as can be directly inferred from Eq. (3).

V. CONCLUSION

We developed a physical model describing spin-wave dynamics in magnetic/nonmagnetic/magnetic heterostructures and benchmarked its predictions against well established micromagnetic simulation platforms. The model captures the essential features of dipolarly coupled spin-wave modes in vertically stacked systems, providing direct access to their dispersion relations, mode hybridization, and symmetry properties. We show how the intrinsic tunability of iron garnets, arising from compositional variability, strain-induced effects, and controllable anisotropy landscapes, could be exploited for systematic tailoring of the collective spin-wave spectrum within the proposed theoretical framework.

The possibility of independently varying the magnetic properties of the two layers, while retaining dipolar coupling as the dominant interaction mechanism, establishes garnet-based heterostructures as a particularly suitable platform for modeling and design studies of collective magnonic phenomena. Beyond fundamental interest, the presented framework provides a predictive and physically transparent tool for the design of functional magnonic elements.

ACKNOWLEDGMENTS

The authors acknowledge valuable discussions with R. Bertacco and F. Maspero. L. M. acknowledges G. Gubbiotti and M. Madami for valuable discussions. O. W. acknowledges support from a Marie Curie Fellowship (Horizon Europe—MSCA Grant Agreement No. 101211677, project FeriMag). C. A. R. and M. J. G. acknowledge support from NSF DMR 2323132. A. D. G. acknowledges support from Politecnico di Milano. S. K. acknowledges support from the Dutch Research Council (NWO) via VI.Veni.222.296.

DATA AVAILABILITY

The data supporting this study can be found in the ZENODO repository [69] and in the Supplemental Material [70].

[1] B. Khurana, A. C. Kaczmarek, C.-T. Chou, T. Su, K. Lasinger, T. Grossmark, D. C. Bono, L. Liu, and C. A. Ross, Rare-earth iron garnet superlattices with sub-unit cell composition modulation, ACS Nano **18**, 35269 (2024).

[2] P. Fourmont, E. Cho, S. G. Cloutier, and C. A. Ross, Exchange bias in $La_{0.67}Sr_{0.33}MnO_3/YFeO_3$ ferromagnet/antiferromagnet multilayer heterostructures, Small **21**, 2501644 (2025).

[3] M. J. Gross, J. Herrero-Martin, S. Valencia, A. J. Grutter, J. A. Borchers, Y. Choi, G. Fabbris, A. C. Kaczmarek, A. E. Kossak, J. J. Bauer *et al.*, Interfacial alloying contributions to the magnetic proximity effect in Pt/dysprosium iron garnet, Phys. Rev. B **112**, 054433 (2025).

[4] J. J. Bauer, P. Quarterman, A. J. Grutter, B. Khurana, S. Kundu, K. A. Mkhoyan, J. A. Borchers, and C. A. Ross, Magnetic proximity effect in magnetic-insulator/heavy-metal heterostructures across the compensation temperature, Phys. Rev. B **104**, 094403 (2021).

[5] Y. Fan, T. Fakhrul, J. T. Hou, C.-T. Chou, B. Khurana, Y. Tserkovnyak, L. Liu, and C. A. Ross, Dynamically tunable magnon-magnon coupling in a perpendicular anisotropy magnetic garnet-ferromagnet bilayer, Phys. Rev. Lett. **134**, 126702 (2025).

[6] H. Wu, C. Wan, X. Zhang, Z. Yuan, Q. Zhang, J. Qin, H. Wei, X. Han, and S. Zhang, Observation of magnon-mediated electric current drag at room temperature, Phys. Rev. B **93**, 060403(R) (2016).

[7] P. Pirro, T. Brächer, A. V. Chumak, B. Lägel, C. Dubs, O. Surzhenko, P. Görnert, B. Leven, and B. Hillebrands, Spin-wave excitation and propagation in microstructured waveguides of yttrium iron garnet/Pt bilayers, Appl. Phys. Lett. **104**, 012405 (2014).

[8] S. Klingler, V. Amin, S. Geprägs, K. Ganzhorn, H. Maier-Flaig, M. Althammer, H. Huebl, R. Gross, R. D. McMichael, M. D. Stiles *et al.*, Spin-torque excitation of perpendicular standing spin waves in coupled YIG/Co heterostructures, Phys. Rev. Lett. **120**, 127201 (2018).

[9] J. Qian, Y. Li, Z. Jiang, R. Busch, H.-C. Ni, T.-H. Lo, A. Hoffmann, A. Schleife, and J.-M. Zuo, Unraveling the origin of antiferromagnetic coupling at YIG/permalloy interface, Phys. Rev. Mater. **8**, 104405 (2024).

[10] Y. Tserkovnyak, A. Brataas, G. E. W. Bauer, and B. I. Halperin, Nonlocal magnetization dynamics in ferromagnetic heterostructures, Rev. Mod. Phys. **77**, 1375 (2005).

[11] M. Althammer, S. Meyer, H. Nakayama, M. Schreier, S. Altmannshofer, M. Weiler, H. Huebl, S. Geprägs, M. Opel, R. Gross *et al.*, Quantitative study of the spin Hall magnetoresistance in ferromagnetic insulator/normal metal hybrids, Phys. Rev. B **87**, 224401 (2013).

[12] H. Nakayama, M. Althammer, Y.-T. Chen, K.-i. Uchida, Y. Kajiwara, D. Kikuchi, T. Ohtani, S. Geprägs, M. Opel, S. Takahashi *et al.*, Spin Hall magnetoresistance induced by a nonequilibrium proximity effect, Phys. Rev. Lett. **110**, 206601 (2013).

[13] F. Millo, J.-P. Adam, C. Chappert, J.-V. Kim, A. Mouhoub, A. Solignac, and T. Devolder, Unidirectionality of spin waves in synthetic antiferromagnets, Phys. Rev. Appl. **20**, 054051 (2023).

[14] R. A. Gallardo, T. Schneider, A. K. Chaurasiya, A. Oelschlägel, S. S. P. K. Arekapudi, A. Roldán-Molina, R. Hübner, K. Lenz, A. Barman, J. Fassbender, J. Lindner, O. Hellwig, and P. Landeros, Reconfigurable spin-wave nonreciprocity induced by dipolar interaction in a coupled ferromagnetic bilayer, Phys. Rev. Appl. **12**, 034012 (2019).

[15] R. A. Gallardo, P. Alvarado-Seguel, A. Kákay, J. Lindner, and P. Landeros, Spin-wave focusing induced by dipole-dipole interaction in synthetic antiferromagnets, Phys. Rev. B **104**, 174417 (2021).

[16] Y.-T. Chen, S. Takahashi, H. Nakayama, M. Althammer, S. T. B. Goennenwein, E. Saitoh, and G. E. W. Bauer, Theory of spin Hall magnetoresistance, Phys. Rev. B **87**, 144411 (2013).

[17] O. Gladii, R. Salikhov, O. Hellwig, H. Schultheiss, J. Lindner, and R. A. Gallardo, Spin-wave nonreciprocity at the spin-flop transition region in synthetic antiferromagnets, Phys. Rev. B **107**, 104419 (2023).

[18] V. V. Kruglyak, S. O. Demokritov, and D. Grundler, Magnonics, J. Phys. D **43**, 264001 (2010).

[19] A. V. Chumak, V. I. Vasyuchka, A. A. Serga, and B. Hillebrands, Magnon spintronics, Nat. Phys. **11**, 453 (2015).

[20] B. A. Kalinikos and A. N. Slavin, Theory of dipole-exchange spin wave spectrum for ferromagnetic films with mixed exchange boundary conditions, J. Phys. C **19**, 7013 (1986).

[21] A. Kreisel, F. Sauli, L. Bartosch, and P. Kopietz, Microscopic spin-wave theory for yttrium-iron garnet films, Eur. Phys. J. B **71**, 59 (2009).

[22] K. Vayhinger and H. Kronmüller, Propagating spin waves in ferromagnetic multilayers, J. Magn. Magn. Mater. **62**, 159 (1986).
[23] I. A. Armijo and R. E. Arias, Spin wave modes of multilayered ferromagnetic films, Phys. Rev. B **99**, 014432 (2019).
[24] B. Hillebrands, Calculation of spin waves in multilayered structures including interface anisotropies and exchange contributions, Phys. Rev. B **37**, 9885 (1988).
[25] M. Vohl, J. Barnaś, and P. Grünberg, Effect of interlayer exchange coupling on spin-wave spectra in magnetic double layers: Theory and experiment, Phys. Rev. B **39**, 12003 (1989).
[26] B. Hillebrands, Spin-wave calculations for multilayered structures, Phys. Rev. B **41**, 530 (1990).
[27] H. Qin, R. B. Holländer, L. Flajšman, F. Hermann, R. Dreyer, G. Woltersdorf, and S. van Dijken, Nanoscale magnonic Fabry-Pérot resonator for low-loss spin-wave manipulation, Nat. Commun. **12**, 2293 (2021).
[28] Q. Wang, P. Pirro, R. Verba, A. Slavin, B. Hillebrands, and A. V. Chumak, Reconfigurable nanoscale spin-wave directional coupler, Sci. Adv. **4**, e1701517 (2018).
[29] K. Szulc and M. Krawczyk, Magnetic field-controlled nanoscale spin-wave vertical directional coupler, Appl. Phys. Lett. **126**, 232404 (2025).
[30] G. Gubbiotti *et al.*, 2025 roadmap on 3D nanomagnetism, J. Phys. Condens. Matter **37**, 143502 (2025).
[31] R. Verba, G. Melkov, V. Tiberkevich, and A. Slavin, Collective spin-wave excitations in a two-dimensional array of coupled magnetic nanodots, Phys. Rev. B **85**, 014427 (2012).
[32] K. Y. Guslienko, S. O. Demokritov, B. Hillebrands, and A. N. Slavin, Effective dipolar boundary conditions for dynamic magnetization in thin magnetic stripes, Phys. Rev. B **66**, 132402 (2002).
[33] K. Y. Guslienko and A. N. Slavin, Boundary conditions for magnetization in magnetic nanoelements, Phys. Rev. B **72**, 014463 (2005).
[34] Q. Wang, B. Heinz, R. Verba, M. Kewenig, P. Pirro, M. Schneider, T. Meyer, B. Laegel, C. Dubs, T. Brächer *et al.*, Spin pinning and spin-wave dispersion in nanoscopic ferromagnetic waveguides, Phys. Rev. Lett. **122**, 247202 (2019).
[35] H. Mortada, R. Verba, Q. Wang, P. Pirro, and A. A. Hamadeh, Nonreciprocal spin waves in out-of-plane magnetized coupled waveguides reconfigured by domain wall displacements, Adv. Electron. Mater. **11**, e00575 (2025).
[36] M. Beleggia, S. Tandon, Y. Zhu, and M. De Graef, On the magnetostatic interactions between nanoparticles of arbitrary shape, J. Magn. Magn. Mater. **278**, 270 (2004).
[37] M. Beg, M. Lang, and H. Fangohr, Ubermag: Toward more effective micromagnetic workflows, IEEE Trans. Magn. **58**, 7300205 (2022).
[38] L. Körber, G. Quasebarth, A. Hempel, F. Zahn, A. Otto, E. Westphal, R. Hertel, and A. Kákay, TetraX: Finite-element micromagnetic-modeling package (2022).
[39] L. Körber, G. Quasebarth, A. Otto, and A. Kákay, Finite-element dynamic-matrix approach for spin-wave dispersions in magnonic waveguides with arbitrary cross section, AIP Adv. **11**, 095231 (2021).
[40] V. Vlaminck and M. Bailleul, Spin-wave transduction at the submicrometer scale: Experiment and modeling, Phys. Rev. B **81**, 014425 (2010).
[41] H. Qin, S. J. Hämäläinen, K. Arjas, J. Witteveen, and S. van Dijken, Propagating spin waves in nanometer-thick yttrium iron garnet films: Dependence on wave vector, magnetic field strength, and angle, Phys. Rev. B **98**, 224422 (2018).
[42] Y.-X. Li, G.-X. La, and G.-P. Zheng, Time-independent perturbation theory of non-Hermitian Hamiltonian, Int. J. Theor. Phys. **64**, 251 (2025).
[43] N. Moiseyev, *Non-Hermitian Quantum Mechanics* (Cambridge University Press, Cambridge, United Kingdom, 2011).
[44] N. Zenbaa, K. O. Levchenko, J. Panda, K. Davídková, M. Ruhwedel, S. Knauer, M. Lindner, C. Dubs, Q. Wang, M. Urbánek *et al.*, YIG/CoFeB bilayer magnonic isolator, IEEE Magn. Lett. **16**, 6100205 (2025).
[45] S. A. Odintsov, S. E. Sheshukova, S. A. Nikitov, E. H. Lock, E. N. Beginin, and A. V. Sadovnikov, Nonreciprocal spin wave propagation in bilayer magnonic waveguide, J. Magn. Magn. Mater. **546**, 168736 (2022).
[46] Z. Jin, H. Zhou, X. Zhang, K. Cao, and R. Chen, Interface-mediated YIG/Ce:YIG bilayers structure with enhanced magneto-optical properties via pulsed laser deposition, ACS Mater. Lett. **5**, 803 (2023).
[47] K. S. Rathore, A. Swain, J. Lim, A. Mishra, P. Gupta, L. Yong Heng, J. Luwen, R. Mahendiran, A. Hoffmann, and S. Bedanta, Magnon-magnon coupling in an all-oxide insulator garnet $Y_3Fe_5O_{12}/Tm_3Fe_5O_{12}$ heterostructure, Phys. Rev. Appl. **25**, 024036 (2026).
[48] S. Wintz, V. Tiberkevich, M. Weigand, J. Raabe, J. Lindner, A. Erbe, A. Slavin, and J. Fassbender, Magnetic vortex cores as tunable spin-wave emitters, Nat. Nanotechnol. **11**, 948 (2016).
[49] E. Albisetti, S. Tacchi, R. Silvani, G. Scaramuzzi, S. Finizio, S. Wintz, C. Rinaldi, M. Cantoni, J. Raabe, G. Carlotti, R. Bertacco, E. Riedo, and D. Petti, Optically inspired nanomagnonics with nonreciprocal spin waves in synthetic antiferromagnets, Adv. Mater. **32**, 1906439 (2020).
[50] D. Girardi, S. Finizio, C. Donnelly, G. Rubini, S. Mayr, V. Levati, S. Cuccurullo, F. Maspero, J. Raabe, D. Petti, and E. Albisetti, Three-dimensional spin-wave dynamics, localization and interference in a synthetic antiferromagnet, Nat. Commun. **15**, 3057 (2024).
[51] Y. Liu, P. Zhou, R. Bidthanapally, J. Zhang, W. Zhang, M. R. Page, T. Zhang, and G. Srinivasan, Strain control of magnetic anisotropy in yttrium iron garnet films in a composite structure with yttrium aluminum garnet substrate, J. Compos. Sci. **6**, 203 (2022).
[52] J. J. Bauer, E. R. Rosenberg, S. Kundu, K. A. Mkhoyan, P. E. Quarterman, A. J. Grutter, B. J. Kirby, J. A. Borchers, and C. A. Ross, Dysprosium iron garnet thin films with perpendicular magnetic anisotropy on silicon, Adv. Electron. Mater. **6**, 1900820 (2020).
[53] T. Fakhrul, B. Khurana, H. T. Nembach, J. M. Shaw, Y. Fan, G. A. Riley, L. Liu, and C. A. Ross, Substrate-dependent anisotropy and damping in epitaxial bismuth yttrium iron garnet thin films, Adv. Mater. Interfaces **10**, 2300217 (2023).

[54] Y. Song, A. C. Kaczmarek, G. S. D. Beach, and C. A. Ross, Engineering an easy-plane anisotropy in an epitaxial europium iron garnet (110) film, Phys. Rev. Mater. **7**, 084407 (2023).

[55] Y. Song, K. Lasinger, H. Tang, J. Li, G. S. D. Beach, and C. A. Ross, Temperature-dependent surface anisotropy in (110) epitaxial rare earth iron garnet films, Small **20**, 2407381 (2024).

[56] E. R. Rosenberg, K. Litzius, J. M. Shaw, G. A. Riley, G. S. D. Beach, H. T. Nembach, and C. A. Ross, Magnetic properties and growth-induced anisotropy in yttrium thulium iron garnet thin films, Adv. Electron. Mater. **7**, 2100452 (2021).

[57] T. Fakhrul, S. Tazlaru, L. Beran, Y. Zhang, M. Veis, and C. A. Ross, Magneto-optical Bi:YIG films with high figure of merit for nonreciprocal photonics, Adv. Opt. Mater. **7**, 1900056 (2019).

[58] A. C. Kaczmarek, E. R. Rosenberg, Y. Song, K. Ye, G. A. Winter, A. N. Penn, R. Gomez-Bombarelli, G. S. D. Beach, and C. A. Ross, Atomic order of rare earth ions in a complex oxide: A path to magnetotaxial anisotropy, Nat. Commun. **15**, 5083 (2024).

[59] E. Rosenberg, J. Bauer, E. Cho, A. Kumar, J. Pelliciari, C. A. Occhialini, S. Ning, A. Kaczmarek, R. Rosenberg, J. W. Freeland *et al.*, Revealing site occupancy in a complex oxide: Terbium iron garnet, Small **19**, 2300824 (2023).

[60] T. Yoshimoto, T. Goto, K. Shimada, B. Iwamoto, Y. Nakamura, H. Uchida, C. A. Ross, and M. Inoue, Static and dynamic magnetic properties of single-crystalline yttrium iron garnet films epitaxially grown on three garnet substrates, Adv. Electron. Mater. **4**, 1800106 (2018).

[61] T. Fakhrul, S. Huang, Y. Song, B. Khurana, G. S. D. Beach, and C. A. Ross, Influence of substrate on interfacial Dzyaloshinskii-Moriya interaction in epitaxial $Tm_3Fe_5O_{12}$ films, Phys. Rev. B **107**, 054421 (2023).

[62] H. Wu, L. Huang, C. Fang, B. S. Yang, C. H. Wan, G. Q. Yu, J. F. Feng, H. X. Wei, and X. F. Han, Magnon valve effect between two magnetic insulators, Phys. Rev. Lett. **120**, 097205 (2018).

[63] A. Barman, G. Gubbiotti, S. Ladak, A. O. Adeyeye, M. Krawczyk, J. Gräfe, C. Adelmann, S. Cotofana, A. Naeemi, V. I. Vasyuchka *et al.*, The 2021 magnonics roadmap, J. Phys. Condens. Matter **33**, 413001 (2021).

[64] P. B. Jayathilaka, M. C. Monti, J. T. Markert, and C. W. Miller, Heterostructures for realizing magnon-induced spin transfer torque, Adv. Condens. Matter Phys. **2012**, 168313 (2012).

[65] S. Li, K. Shen, and K. Xia, Magnon hybridization in ferrimagnetic heterostructures, Phys. Rev. B **102**, 224413 (2020).

[66] Z. Li, S. Jiang, F. Li, Y. Fan, Q. Wang, T. Zhang, Q. Zhao, J. Wang, Q. Liu, G. Yu, Y. Peng, J. Zhang, and J. Wei, Propagating spin wave in perpendicularly magnetized TmIG/MgO/TmIG trilayer for magnonic band-stop filters, Adv. Funct. Mater. **36**, e26781 (2025).

[67] C. Guo, C. Wan, X. Wang, C. Fang, P. Tang, W. Kong, M. Zhao, L. Jiang, B. Tao, G. Yu *et al.*, Magnon valves based on YIG/NiO/YIG all-insulating magnon junctions, Phys. Rev. B **98**, 134426 (2018).

[68] C. H. Truong, J.-H. An, P. Cao Van, and J.-R. Jeong, Optimization of YIG/Pt/YIG magnon valve structures for magnetic memory applications, Korean J. Mater. Res. **34**, 560 (2024).

[69] A. Del Giacco, L. Menna, M. J. Gross, O. Wojewoda, V. Levati, M. Urbanek, S. Kurdi, E. Albisetti, D. Petti, and C. A. Ross, Data for "Reciprocal space approach to dipolarly coupled magnetic heterostructures, Zenodo (2026).

[70] See Supplemental Material at http://link.aps.org/supplemental/10.1103/9z24-jjx3 for additional simulations and extended mathematical derivations.